JOURNAL OF APPLIED PHYSICS **109**, 123515 (2011)

In situ analysis of elemental depth distributions in thin films by combined evaluation of synchrotron x-ray fluorescence and diffraction

R. Mainz[a] and R. Klenk
Helmholtz-Zentrum Berlin, Hahn-Meitner-Platz 1, D-14109 Berlin, Germany

(Received 23 December 2010; accepted 15 April 2011; published online 21 June 2011; publisher error corrected February 13, 2012)

In this work we present a method for the *in situ* analysis of elemental depth distributions in thin films using a combined evaluation of synchrotron x-ray fluorescence and energy-dispersive x-ray diffraction signals. We recorded diffraction and fluorescence signals simultaneously during the reactive annealing of thin films. By means of the observed diffraction signals, the time evolution of phases in the thin films during the annealing processes can be determined. We utilized this phase information to parameterize the depth distributions of the elements in the films. The time-dependent fluorescence signals were then taken to determine the parameters representing the parameterized depth distributions. For this latter step, we numerically calculated the fluorescence intensities for a given set of depth distributions. These calculations handle polychromatic excitation and arbitrary functions of depth distributions and take into account primary and secondary fluorescence. Influences of lateral non-uniformities of the films, as well as the accuracy limits of the method, are investigated. We apply the introduced method to analyze the evolution of elemental depth distributions and to quantify the kinetic parameters during a synthesis process of $CuInS_2$ thin films via the reactive annealing of Cu–In precursors in a sulfur atmosphere. © *2011 American Institute of Physics*. [doi:10.1063/1.3592288]

I. INTRODUCTION

Reactive thin film formation processes have undergone rapid development in recent years. The development has been accelerated by a growing thin film photovoltaic industry and the demand for fast film formation processes. In order to further increase the efficiency of thin film fabrication, it is essential to obtain detailed information about the reactions taking place within the films during the formation processes. Currently, the study of the formation processes of films consisting of chalcopyrite $Cu(In_{1-x}Ga_x)(S_{1-y}S_y)_2$ (or, in shorthand, $Cu(In,Ga)(S,Se)_2$) used as absorbers for thin film solar cells is a subject of intense research. Most fabrication processes of $Cu(In,Ga)(S,Se)_2$ absorber films consist of a multi-stage process design. The highest energy conversion efficiencies for thin film solar cells are obtained with $Cu(In,Ga)Se_2$ (CIGSe) absorber films prepared in a multi-stage physical vapor deposition process.[1–3] An alternative and faster method for the synthesis of $Cu(In,Ga)(S,Se)_2$ films with promising conversion efficiencies is the reactive annealing of metallic precursors in chalcogen vapor by rapid thermal processing.[1,4]

These types of processes present reaction-diffusion systems in which the elements diffuse through at least a part of the film in order to react with other elements. As a consequence, the depth distributions of the involved elements undergo constant change during reactive film formation. In order to understand and control the reactive film growth, it is desirable to gain information about both the formation of phases and the evolution of elemental depth distributions *in situ*. The evolution of elemental depth distributions during $Cu(In,Ga)(S,Se)_2$ film formation processes has been studied by several authors by interrupting the formation process and analyzing the depth distributions using *ex situ* methods such as energy-dispersive x-ray spectroscopy,[5] scanning auger spectroscopy,[6] secondary neutral mass spectrometry,[7] and glow discharge optical emission spectroscopy.[8] The suitability of *ex situ* grazing incidence x-ray fluorescence for the high-resolution determination of graded depth profiles in thin films has recently been investigated by Streeck *et al.*[9] Although *ex situ* methods usually feature good spatial resolutions of depth distributions, a high time resolution is necessarily connected with time-consuming experimental effort, because a single process has to be performed for each point in time at which depth distributions are to be analyzed. Moreover, due to possible influences of the interruption procedure, it is usually unknown how well the state of a sample at room temperature represents the state at elevated temperatures when the process was interrupted. Additionally, a high degree of reproducibility of a process is necessary in order to obtain a consistent series of sample states representing the evolution of depth distributions during the process.

In this paper, we introduce a new approach for the *in situ* analysis of elemental depth distributions during reactive film formation processes. We exploit the fact that in energy-dispersive x-ray diffraction (EDXRD), diffraction signals and fluorescence signals, are measured simultaneously.[10] EDXRD has been used for several years and is well established for analyzing phase formations during reactive film growth processes.[10–15] *In situ* fluorescence signals recorded during EDXRD measurements have been discussed as indications for changes of depth distributions.[10,16] Also,

[a]Author to whom correspondence should be addressed. Electronic mail: roland.mainz@helmholtz-berlin.de.

 © 2011 American Institute of Physics

in situ fluorescence signals have been used to monitor the evaporation of elements off of the substrate, e.g., Sn loss during kesterite (Cu_2ZnSnS_4) film formation.[17] However, the *in situ* analysis of depth distributions with the help of quantitatively calculated fluorescence intensities has not been reported before. The intensities of the fluorescence signals are influenced by the depth distributions of the elements due to attenuation of the incident radiation and the emitted radiation within the film. Our approach is to calculate the fluorescence intensities for a given set of parameterized depth distributions of all of the constituting elements, and to model the depth distributions of these elements by minimizing the deviation of the calculated from the measured fluorescence intensities. The calculation of the fluorescence intensities is described in Sec. II. The influence of the different elemental cross sections is discussed, and the contribution of the secondary fluorescence is investigated. For the modeling of the depth distributions, the depth distributions need to be expressed by a limited number of parameters. In Sec. III, the parameterization model is presented, and the influence of lateral inhomogeneities on the fluorescence signals is investigated. Finally, we demonstrate the potential of the method by applying it to experimental data recorded during a $CuInS_2$ (CIS) synthesis process involving the reactive annealing of a Cu–In precursor in sulfur vapor (Sec. IV). The application of the presented method to experimental data recorded during the synthesis of $Cu(In,Ga)S_2$ (CIGS) will be published elsewhere.

II. FLUORESCENCE INTENSITIES

The only factors that influence the fluorescence intensities during an *in situ* measurement of a reactive process with a fixed detector setup are the amounts and depth distributions of the elements in the sample (besides experimental factors such as intensity variations of the incident radiation, which are canceled out by using relations between different signal intensities). In order to extract these properties from fluorescence measurements, we calculate the fluorescence intensities for a given film characterized by its composition, its thickness, and the depth distributions. For the calculation of the fluorescence intensities, we developed a numerical code that can handle polychromatic excitation (as needed for the use of polychromatic synchrotron radiation). The code calculates Kα and Kβ fluorescence intensities for arbitrary depth distributions and takes into account primary and secondary fluorescence. The formulas for the calculation of the primary and secondary fluorescence intensities for inhomogeneous samples with polychromatic excitation are given in Appendix A.

A. Atomic cross-sections for x-rays

The sensitivity of the presented method depends on the variation of the fluorescence intensities with a variation of the depth distributions. This sensitivity is influenced by the atomic cross-sections of the constituting elements. In Fig. 1, the total atomic cross-sections σ of the constituents of $Cu(In,Ga)(S,Se)_2$ and Mo are displayed as functions of the photon energy. The lower a cross-section is for a given photon energy, the higher the depth of penetration, and the less

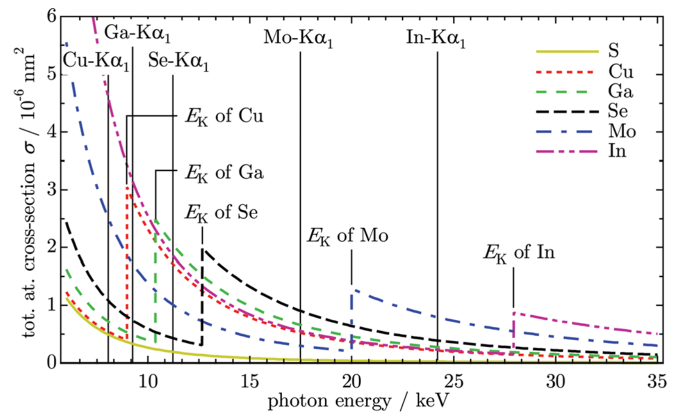

FIG. 1. (Color online) Total atomic cross-sections of the elements S, Cu, Ga, Se, Mo, and In. The vertical lines mark the energies of the Kα_1 transitions. E_K denotes the K-shell absorption edge (source: Ref. 42).

the corresponding fluorescence intensity is influenced by a change of the depth distributions. Above the K-edge of In, as well as at the energy of In-Kα, the cross-sections of the other elements are very small. As a consequence, a change of the In distribution has only a small influence on the In-Kα intensity. In contrast, at the energy of Ga-Kα, the cross-sections of In and Cu are large. Therefore, the signal of Ga-Kα strongly varies with a change in the Cu, In, and Ga distributions. The fact that the signal for Cu-Kα also is strongly attenuated by In leads to a high sensitivity to changes in the In and Cu distributions.

B. Contribution of secondary fluorescence

In the following, we investigate the role of the secondary fluorescence for the case of thin films consisting of Cu, In, Ga, S, and Se and argue that the ternary fluorescence can be neglected. The calculation of the contribution of secondary fluorescence to the total fluorescence intensity increases the computation time significantly. In order to examine the importance of the secondary fluorescence, the ratio between the secondary fluorescence and the primary fluorescence is calculated for different absorber layers in the $Cu(In,Ga)(S,Se)_2$ system. The results of these calculations are presented in Fig. 2. For a CIS/Mo layer stack (Fig. 2(a)) with a CIS layer thickness greater than 1 μm, mainly the Mo-Kα fluorescence is influenced by secondary fluorescence (caused by excitation by the primary In-Kα fluorescence). The secondary Cu-Kα fluorescence is low because the cross-section of Cu is small at the energies of In-Kα and Mo-Kα (see Fig. 1). If the layer contains Ga (Fig. 2(b)), the secondary fluorescence of Cu-Kα increases, because at the energy of Ga-Kα the cross-section of Cu is large. In the cases of $CuInSe_2$ (CISe; Fig. 2(d)) and $Cu(In,Ga)Se_2$ (CIGSe; Fig. 2(e)), the secondary fluorescence for Cu-Kα and Ga-Kα is higher than that for CIS and CIGS. This is due to the fact that the energy of Se-Kα is above the K-shell absorption edges of Cu and Ga, whereas the energy for S-Kα is below these absorption edges. The values for Figs. 2(a), 2(b), 2(d), and 2(e) were calculated for the polychromatic radiation of the F3 beamline at HASYLAB. The spectrum of the incident radiation influences the contribution of the secondary fluorescence. In Figs. 2(c) and 2(f), the

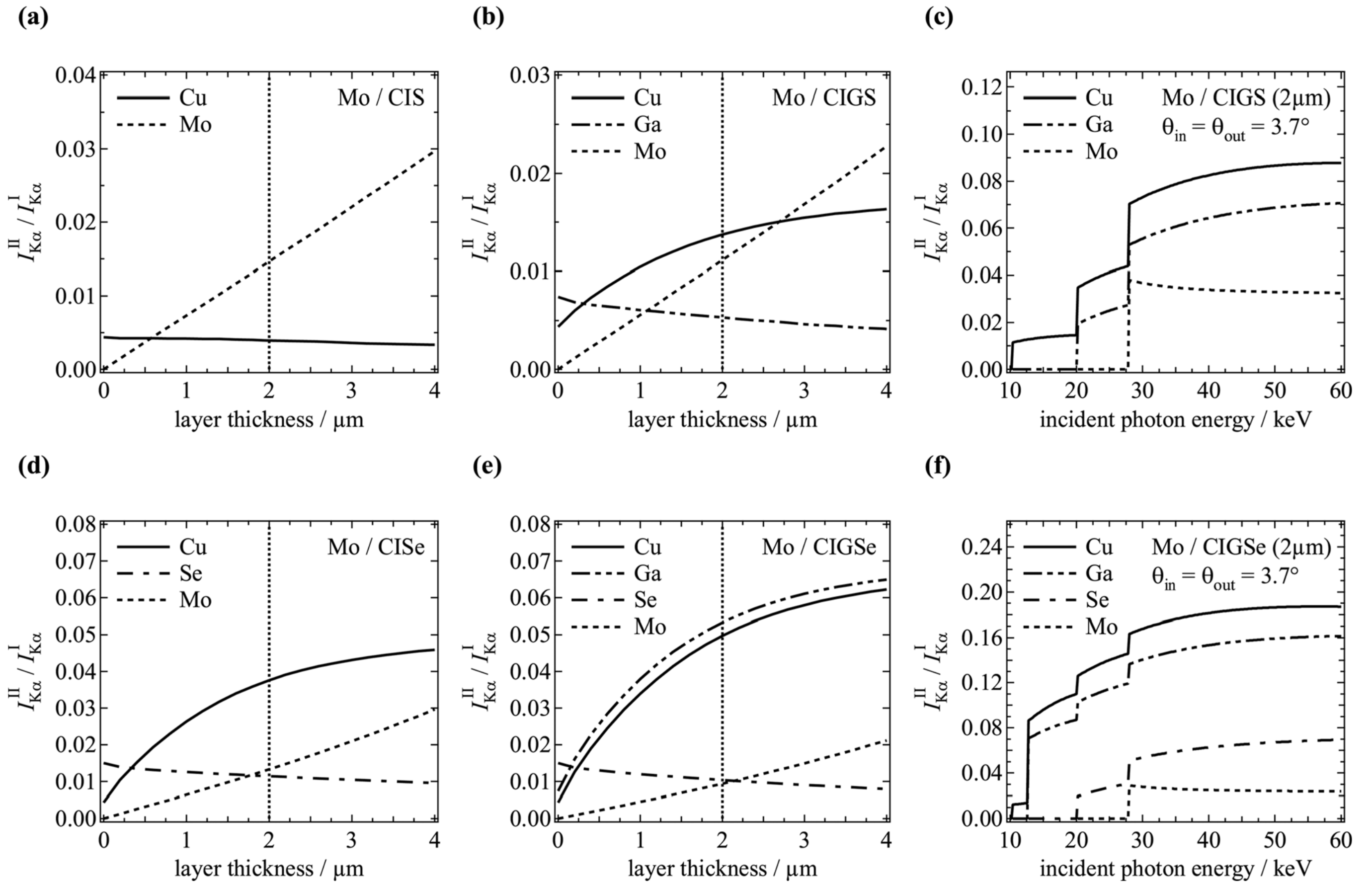

FIG. 2. Calculated ratios between the intensities of the secondary and primary Kα fluorescence for different chalcopyrite absorber layers on a 500 nm thick Mo layer. The graphs in (a), (b), (d), and (e) show the ratios between the secondary and primary fluorescence as functions of the chalcopyrite layer thickness for (a) $CuInS_2$ (CIS), (b) $Cu(In_{1-x}Ga_x)S_2$ with $x = 0.24$ (CIGS), (d) $CuInSe_2$(CISe), and (e) $Cu(In_{1-x}Ga_x)Se_2$ with $x = 0.3$ (CIGSe). The vertical lines mark a typical thickness (2 μm) of the chalcopyrite films. The values in (a), (b), (d), and (e) were calculated with the polychromatic radiation of the F3 beamline at HASYLAB as incident radiation and with an incident and exit angle of 3.7°. The graphs in (c) and (f) show the ratios between the secondary and primary fluorescence as functions of the energy of the incident radiation for a fixed layer thickness (2 μm) for (c) $Cu(In_{1-x}Ga_x)S_2$ with $x = 0.24$ and (f) $Cu(In_{1-x}Ga_x)Se_2$ with $x = 0.3$.

dependence of the contributions of the secondary fluorescence on the energy of the incident photons (monochromatic radiation) is depicted for the layer stacks CIGS/Mo and CIGSe/Mo.

For the polychromatic radiation of the F3 beamline at HASYLAB and for the case of CIS and CIGS with a typical layer thickness of 2 μm, the contribution of secondary fluorescence can reach up to 3%. We conclude that it is necessary to include the secondary fluorescence in our calculations. The ratio between ternary and secondary fluorescence can be expected to be roughly of the same order of magnitude as the ratio between secondary and primary fluorescence. With the help of Fig. 2, the ternary fluorescence is estimated to be on the order of 0.1% for polychromatic excitation and is neglected for the modeling presented in this work. However, if a very high accuracy is needed, the ternary fluorescence might have to be considered in certain cases, especially with monochromatic excitation with high energies.

III. PARAMETERIZATION OF DEPTH DISTRIBUTIONS

In order to model the elemental depth distributions, they have to be represented by a limited number of parameters that must not exceed the number of measured fluorescence signals. Because the *in situ* measurements were performed with a single detector under a fixed angle, only a small number of distinct fluorescence signals were available for the determination of the elemental distributions. To find a suitable parameterization, the solid phases present in the film (determined by the diffraction signals) were utilized in order to reduce the number of parameters representing the elemental depth distributions.

A. The model of homogeneous plane-parallel layers

As a first restriction for the elemental distributions, lateral uniformity of the composition is assumed, meaning that the atomic densities ρ of the elements are functions of only the sample depth z. The depth distribution of an element l is represented by the function $\rho_l(z)$. Furthermore, it is assumed that the total amount of atoms for each element l within the sample, expressed by the atomic area density

$$\tau_l = \int_{z=0}^{z=d} dz \rho_l(z), \tag{1}$$

is known (d is the total thickness of the sample). (This assumption does not apply to the sulfur in the process presented in Sec. IV.) Additionally, we assume that a finite

number of N different phases are present in the sample and that each phase forms a homogeneous, plane-parallel layer. Consequently, the number of phases N equals the number of layers. This restriction leads to a step function of the atomic densities:

$$\rho_l(z) = \begin{cases} \rho_{1,l}, & z_0 \leq z < z_1 \\ \vdots & \\ \rho_{n,l}, & z_{n-1} \leq z < z_n \\ \vdots & \\ \rho_{N,l}, & z_{N-1} \leq z < z_N, \end{cases} \quad (2)$$

where $z_n - z_{n-1} = \Delta z_n$ is the thickness of layer n. The atomic area density of element l in layer n is then $\tau_{n,l} = \rho_{n,l} \cdot \Delta z_n$, and the sum of the area densities of all layers gives the total area density of the sample: $\Sigma_{n=1}^{N} \tau_{n,l} = \tau_{\text{tot},l}$. Therefore, in a system with N homogeneous layers, there are $N-1$ free parameters per element (represented by $\tau_{n,l}$) for the distribution of the total number of atoms to the N layers. Thus, for L elements the number of independent parameters is $L(N-1)$.

In order to further restrict the number of free parameters for the depth distributions, we make use of the knowledge of the chemical compounds (phases), which are observed by the help of diffraction signals in the EDXRD spectra, and we assign each of the observed phases to a single layer. The stoichiometry of a phase gives the ratio between the elements within the layer. Therefore, the ratio of atomic densities within this layer also is known. From this follows a further reduction of $L-1$ free parameters for each of the N layers. The total number of free parameters necessary to describe a set of depth distributions with the mentioned restrictions is therefore

$$f = L(N-1) - N(L-1) = N - L. \quad (3)$$

The value f gives the number of free parameters that are not determined by the phase information and the area density of the elements. If the sample is in a state in which the number of present phases equals the number of elements with known total atomic area densities, the number of free parameters is zero. Then the amount of atoms (expressed in atomic area densities $\tau_{n,l}$) for each element in each layer can be calculated (see Appendix B1) and the stacking sequence of the layers can be determined by comparing the calculated fluorescence intensities for all possible stacking sequences to the measured intensities.

The thickness of a layer results from the atomic densities and the atomic area densities of the phase in that layer: $d_n = \tau_n / \rho_n$. The atomic densities for the observed phases were calculated from literature data. Table I lists the atomic densities of the phases observed during the sulfurization process investigated in this work. In the presented model, we assume that the compositions of the phases are stoichiometric. According to the relevant phase diagrams,[18–21] the widths of the homogeneity ranges for the phases observed in this work lie between 0 and 3 at.%.

TABLE I. Atomic densities ρ of the phases observed in this work. The values were calculated from the crystallographic structures given in the references. For the calculation of the atomic density for $Cu_{16}In_9$, no reliable data could be found in the literature. Laves and Wallbaum (Ref. 22) identified a partially filled Ni_2In structure of the space group $P6_3mmc$ with $V_{EZ} = 0.083\,\text{nm}^3$. The value in the table assumes a partially filled structure. The digenite phase Cu_2S is usually denoted by $Cu_{1-x}S$; the stoichiometry deviation x is neglected in this work. We note that other intermediate phases can occur during sulfurization, if the process conditions are changed (Refs. 15 and 23).

Phase	Atoms per unit cell	ρ (nm^{-3})
Cu	4	85.1 (Ref. 24)
In	2	38.2 (Ref. 25)
$CuIn_2$	12	50.2 (Ref. 26)
$Cu_{11}In_9$	20	59.9 (Ref. 27)
$Cu_{16}In_9$	6	67 (Ref. 22)
Cu_7In_3	40	68.1 (Ref. 28)
$CuInS_2$	16	47.1 (Ref. 29)
CuS	12	59.1 (Ref. 30)
Cu_2S	12	67.3 (Ref. 31)
Mo	2	64.5 (Ref. 24)

B. The phase mixing model

Because in general there is no reason to assume that during the investigated reaction processes all phases in the sample exist in plane-parallel, uniform layers, in the next step we allow intermixing of two adjacent layers, resulting in depth distributions with composition gradients. This phase intermixing shall represent three different cases:

- In the system Cu–In–Ga–S, a mixing of $CuInS_2$ and $CuGaS_2$ with continuous variation of the composition with the sample depth occurs.[5,7]
- A mixing of the crystal grains of two phases would lead to a three-dimensional distribution of the phases (Fig. 3). Such mixing will be approximated by depth dependent distributions with lateral uniformity. Due to the flat incident and exit angle (3.7°), the radiation encounters several of the grains of each phase according to their volume fractions. This can be very well approximated by assuming a laterally homogeneous mixture of these two phases.
- Also, a rough interface between two adjacent phases leads to a three-dimensional distribution of the phases. It is demonstrated in Sec. III C that a corrugated interface can be approximated by a linear variation of the elemental distributions with the sample depth.

The mixing of two phases (here denoted as phase A and phase B) is expressed by a depth dependent weighing factor

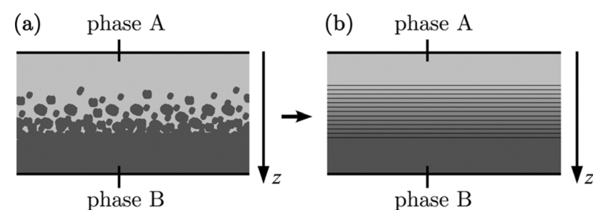

FIG. 3. Mixing of the crystallites of two phases (left) and approximation by a depth dependent distribution with lateral uniformity (right).

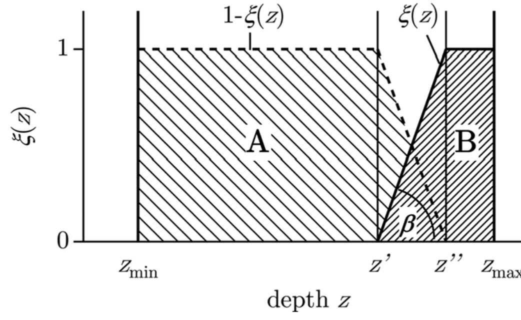

FIG. 4. Illustration of the mixing of two phases. $\xi(z)$ and $1-\xi(z)$ are weighting factors for phases A and B, which give the concentration of the phases in the sample as a function of the depth z.

$\xi(z)$ with $0 \le \xi \le 1$ (z is the distance from the sample surface). If $\xi(z)=0$, only phase A is present at depth z; if $\xi(z)=1$, only phase B is present at depth z. For the case of the mixing of $A = CuInS_2$ and $B = CuGaS_2$, this corresponds to the formula $Cu(In_{1-\xi}Ga_{\xi})S_2$. The total atomic density of a phase mixture is

$$\rho(z) = (1-\xi(z)) \cdot \rho_A + \xi(z) \cdot \rho_B, \quad (4)$$

where ρ_A and ρ_B are the atomic densities of phases A and B, respectively (assuming that the densities follow Vegard's law).

To ensure that the number of parameters describing the depth distributions with phase mixing does not exceed the number of measured fluorescence signals, we choose a simple mixing model with linear gradients. The mixing of two adjacent layers can then be represented by a single parameter. A constraint for the mixing is that the total area densities of the elements are left unchanged by the mixing.

The range of the z-axis in which the two phases are present is divided into three sections (see Fig. 4). In the first section ($z_{min} \le z \le z'$), the parameter $\xi(z)$ equals zero (only phase A is present). In the mixing section ($z' < z < z''$), $\xi(z)$ is a linear function of z (phases A and B are present as a mixture). In the third section ($z'' \le z \le z_{max}$), $\xi(z)$ equals 1 (only phase B is present). If the amount of atoms in the individual phases is fixed, the function $\xi(z)$ depends only on the gradient

$$b = 1/(z'' - z') \quad (5)$$

in the transition zone. Due to a more convenient handling, instead of b we use the mixing parameter β, defined as

$$\beta = \arctan(b \cdot \mu\text{m}). \quad (6)$$

The range of β reaches from $-\pi/2$ ($b=-\infty$) to $+\pi/2$ ($b=+\infty$). A mixing parameter of $\beta=+\pi/2$ describes a system of two adjacent layers with no intermixing; $\beta=0$ describes a complete mixing of two adjacent layers leading to a single homogeneous layer; $\beta=-\pi/2$ also describes two separated, unmixed layers, but with a flipped layer sequence as compared to $\beta=+\pi/2$.

C. Effect of corrugated interfaces on fluorescence intensities

The mixing model introduced in the preceding section assumes the lateral uniformity of the elemental distributions.

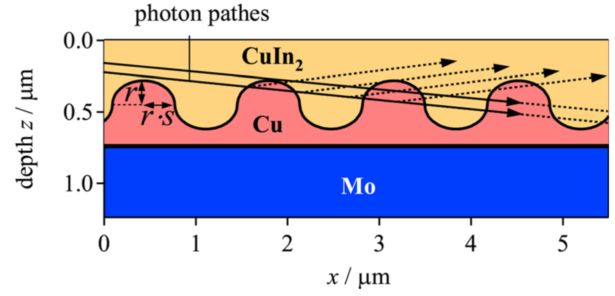

FIG. 5. (Color online) Layer stack consisting of Mo, Cu, and $CuIn_2$ with a corrugated interface between the Cu and $CuIn_2$ layers. For the calculation of the total fluorescence intensities, all possible photon paths have to be considered.

In this section we analyze the effect of a lateral nonuniformity caused by corrugated interfaces between the distinct phases on the fluorescence intensities. In order to do so, we examine an interface described by a periodical function consisting of a series of joint semicircles. The interface model is visualized in Fig. 5 for an interface between a Cu and a $CuIn_2$ layer. We calculated the fluorescence intensities for this structure by numerically integrating over all possible photon paths.

In order to investigate the effect of the shape of the interface on the fluorescence intensities, the shape was modified by varying the radius r and by laterally stretching the interface curve by a factor s (see Fig. 5). The case of $r=0$ leads to a flat interface; at $r=0.28\,\mu$m, the Cu layer starts to form separated islands. Typical scales of roughness are on the order of $0.2\,\mu$m. The stretching factor s simply varies the lateral scale of the shape of the corrugated interface. In the limit $s \to 0$, the lateral inhomogeneity vanishes and the sample becomes laterally uniform. Figure 6 shows the calculated intensity of Cu-Kα relative to the flat case as a function of the parameters r and s. Although a significant dependence of the fluorescence signals on the parameter r can be seen, the dependence on the stretching parameter s is very small. The dependence of the In-Kα on s is even smaller (not shown here).

Further, we examined whether the shape of the interface as depicted in Fig. 5 can be distinguished from a linear transition according to the linear mixing model described in

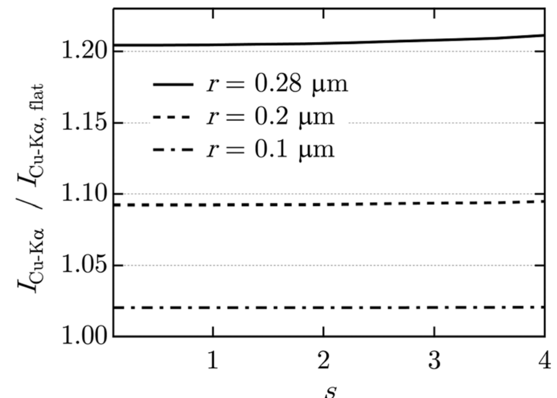

FIG. 6. Dependence of the intensity of Cu-Kα on the parameters r (depth of the interface roughness) and s (lateral stretching of the shape of the corrugated interface). $I_{Cu-K\alpha,flat}$ refers to the case of a flat interface with $r=0$.

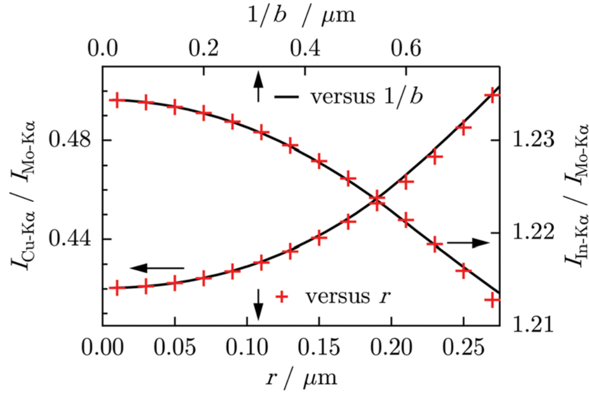

FIG. 7. (Color online) Comparison of the dependence of the intensities of Cu-Kα and In-Kα on the parameter r of the model with corrugated interface (crosses) and on the parameter $1/b$ of the model with linear mixing (solid black line) for the layer sequence $CuIn_2$/Cu/Mo.

Sec. III B. To do so, we used the limit $s \rightarrow 0$ and calculated the fluorescence intensities as a function of the parameter r. Additionally, we calculated the fluorescence intensities with the linear mixing model as a function of the linear mixing parameter b defined in Eq. (5). The results are compared in Fig. 7. The values for the linear mixing are plotted against $1/b$ (solid black line), and the axis is scaled so as to obtain a maximum match with the calculated values for the corrugated interface (crosses). The graph reveals that the two models show a very similar effect on the intensities of the fluorescence signals.

We conclude that lateral inhomogeneities cannot be resolved with the introduced method. The low dependence of the fluorescence intensities on lateral inhomogeneities justifies the restriction to a model with only depth dependent elemental distributions. As a consequence of the similar behavior of the two analyzed interface models, we conclude that we cannot distinguish between different shapes of gradients in the depth distributions.

IV. MODELING OF DEPTH DISTRIBUTIONS DURING CUINS$_2$ SYNTHESIS

In this section, we apply the introduced method for the modeling of depth distributions to the case of CIS synthesis during the sulfurization of an In/Cu/Mo/glass precursor.

A. Experimental details

The precursor was prepared via DC magnetron sputtering from metallic targets onto Mo-coated soda-lime glass. The nominal layer thicknesses for the Mo, Cu, and In layers were 500 nm, 440 nm, and 650 nm, respectively. The amount of material deposited was controlled by weighing, which confirmed an atomic ratio of $[Cu]/[In] = 1.5 \pm 0.05$. The sulfurization was carried out in a vacuum chamber that was attached to the F3 beamline for energy-dispersive diffraction at the HASYLAB synchrotron facility. The chamber is equipped with windows for the incident and diffracted radiation, a sample heater, and a Knudsen type sulfur source. The sulfur partial pressure was controlled by the temperature of the source. The diffracted radiation was recorded with an

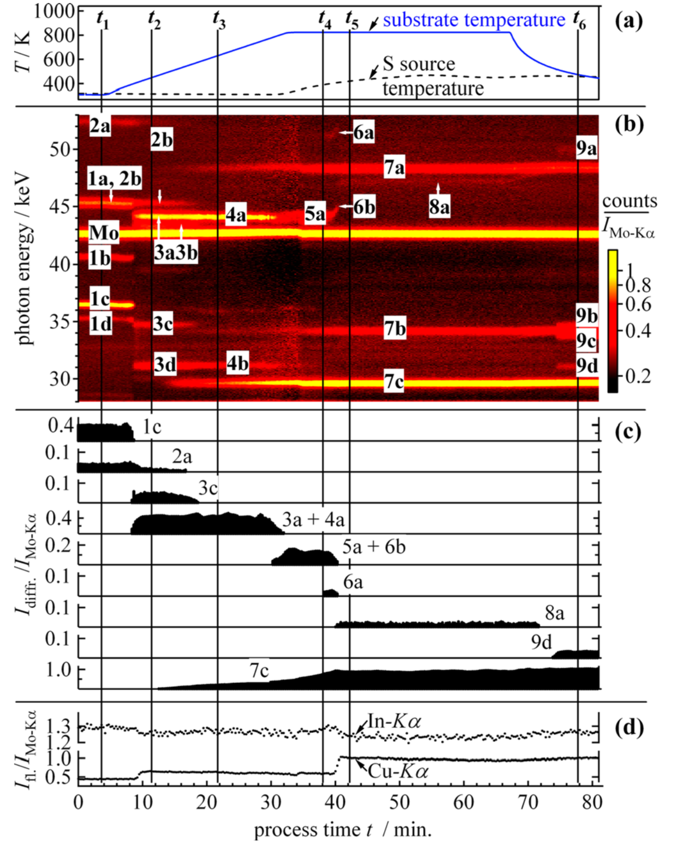

FIG. 8. (Color online) *In situ* measurement of diffraction and fluorescence signals during the $CuInS_2$ synthesis via reactive annealing of Cu–In precursors in a sulfur atmosphere. (a) Temperature profiles of the substrate and of the sulfur source. (b) Color-coded signal intensities vs energy and time. Only the energy range containing the diffraction signals is shown. The maxima were attributed to the following phases and lattice planes. $CuIn_2$; 1a: (202)/(310), 1b: (112)/(220), 1c: (211), 1d: (002). Cu; 2a: (200), 2b: (111). $Cu_{11}In_9$; 3a: (20–2)/(313)/(511), 3b: (11–2), 3c: (312), 3d: (002)/(402)/(11–1)/(311). $Cu_{16}In_9$; 4a: (102)/(110), 4b: (101). 5a: Cu_7In_3 (hkl unclear). $Cu_{1-x}In_x$ (solid solution of In in Cu); 6a: (200), 6b: (111). $CuInS_2$; 7a: (220)/(204), 7b: (200)/(004), 7c: (112). 8a: Cu_2S (220). CuS; 9a: (110)/(107), 9b: (006), 9c: (103), 9d: (102). (c) Integrated relative signal intensities for selected diffraction signals (I_{diffr}) and (d) relative Kα fluorescence signal intensities (I_{fl}) for Cu and In. The diffraction angle for the measurement was $2\theta = 7.500° \pm 0.004°$.

energy-dispersive high purity Ge detector in an energy range from 6 to 57 keV. Further details on the experimental method can be found in Refs. 12, 14, and 32. Spectra for the *in situ* measurements were taken every 20 seconds. All spectra were divided by the intensity of the Mo-Kα fluorescence signal in order to cancel out overall intensity variations.

B. Results

Results of the *in situ* measurements during the $CuInS_2$ synthesis are presented in Fig. 8. The upper part (a) shows the applied temperature profiles for the substrate and the sulfur source. In the middle part (b), the energy and time dependent spectra recorded during the process are depicted (only the energy range containing the diffraction signals is shown). The attribution of the diffraction signals to phases is done according to Refs. 10, 12, 13, and 32. The area intensities of single maxima in the spectra were determined by fitting the maxima in each spectrum to a Gaussian profile.

Because the depth distributions influence the Kα and Kβ signals in a very similar manner, only the sum of Kα_1 and Kα_2 signals was used for the depth profile modeling. In the lower part of the graph, the intensities of diffraction (Fig. 8(c)) and fluorescence signals (Fig. 8(d)) are plotted against the process time.

The evolution of the intensities of the diffraction signals reveals that the metallic phases of the precursor go through several phase transitions. Due to a copper excess with respect to the $CuInS_2$ stoichiometry, the Cu to In ratio of the metallic phases increases while the $CuInS_2$ phase is growing. Once all of the In is consumed for the growth of $CuInS_2$ (at $t \approx 40$ min), the excess Cu reacts with sulfur from the gas phase to form $Cu_{2-x}S$ (we neglect the stoichiometry deviation x in the following and abbreviate this phase as Cu_2S). During the temperature decrease at the end of the process, Cu_2S transforms to CuS.

The observed phases were used for the parameterization of the elemental depth distributions according to the model described in Sec. III. Subsequently, the parameters of these distributions were determined by fitting the calculated fluorescence intensities to the measured fluorescence intensities (see the next section).

C. Modeling of depth distributions

The modeling of depth profiles was performed for several points in time of the sulfurization process presented in the preceding section. In order to explain the modeling procedure, we start with a detailed description for the case of the first investigated point in time (t_1).

(1) The amounts of atoms for the elements in each of the observed phases (Cu, $CuIn_2$, and Mo—see Fig. 8 at t_1) were calculated as described in Sec. IV B. (2) Assuming that each phase forms a single layer, the thicknesses of these layers were calculated from the given amounts of atoms and the atomic densities of each phase (listed in Table I). (3) The sequence of these layers was varied (Figs. 9(a) and 9(c)), and for each sequence the fluorescence intensities were calculated (Figs. 9(b) and 9(d)). The calculated intensities were compared with the fluorescence intensities measured at process time t_1. A comparison of Figs. 9(b) and 9(d) reveals that for the sequence $CuIn_2$/Cu/Mo, the calculated fluorescence intensities fit significantly better to the measured intensities than for the sequences with a flipped layer sequence. (4) By allowing a partial mixing between the phases Cu and $CuIn_2$ according to the model introduced in Sec. III B, the match between the calculated and measured intensities can be further increased (Figs. 9(e) and 9(f)); however, the differences between Figs. 9(d) and 9(f) are small.

In order to find the mixing parameter leading to the best match between the calculated and measured intensities and to investigate the accuracy of the determination of the mixing parameter, we calculated the fluorescence intensities as functions of the mixing parameter β. The result is depicted in the upper left graph of Fig. 10 (the horizontal lines mark the values of the measured intensities). Here, the value of $\beta = -\pi/2$ corresponds to the unmixed layer sequence depicted in Fig. 9(a), the value of $\beta = \pi/2$ corresponds to

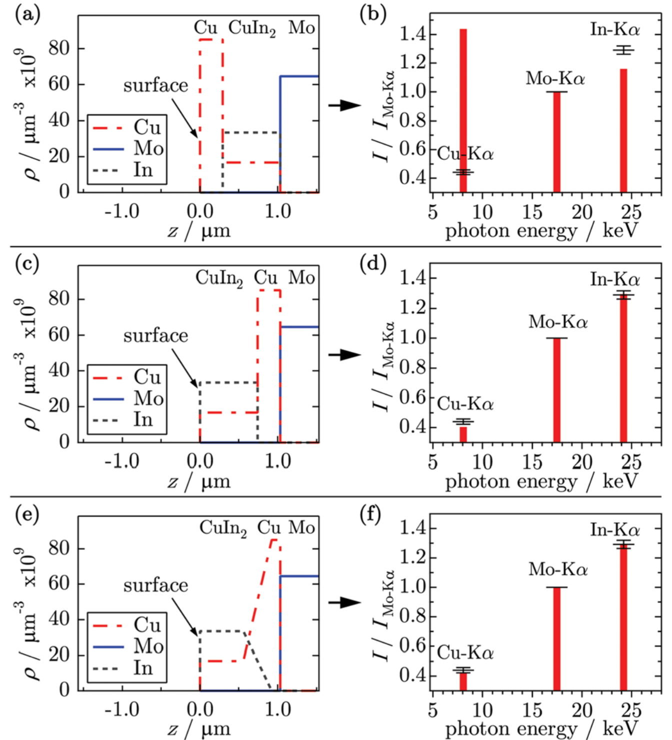

FIG. 9. (Color online) The effect of the layer sequence on the fluorescence intensities. (a) Depth distributions for the layer sequence Cu/$CuIn_2$/Mo. Depicted are the atomic densities of Cu, Mo, and In vs the layer depth z (distance from the surface). (b) Relative fluorescence intensities calculated from the depth distributions shown in (a). The vertical bars mark the calculated relative intensities, and the horizontal black lines mark the measured relative intensities and their standard deviation. (c) Depth distributions for which the sequence of Cu and $CuIn_2$ was flipped as compared to (a). (d) Fluorescence intensities resulting from the depth distributions in (c). (e) Layer sequence with a mixing region between $CuIn_2$ and Cu with a mixing parameter $\beta = 0.4\pi$. (f) Fluorescence intensities resulting from the depth distributions in (e). The values were calculated for polychromatic excitation and an incident and exit angle of 3.7°.

the unmixed layer sequence depicted in Fig. 9(c), and $\beta = 0$ corresponds to a complete, homogeneous mixture of the phases. The shaded region marks the confidence interval of the mixing parameter, which was determined from a variation of the fluorescence signal intensities by the error limits of the measurement. It can be seen that within the confidence interval the calculated values are close to the measured values, whereas outside the confidence interval the deviation between calculated and measured values strongly increases. In the upper center graph of Fig. 10, the error square χ^2 (determined from the difference between the calculated and measured fluorescence intensities) is plotted against β. The top right graph presents the atomic densities of the elements versus the sample depth z with a mixing region that results from the mean value of the mixing parameter within the confidence interval ($\beta = 0.4\pi$).

Figure 10 shows the modeling results of all of the investigated points in time (t_1 to t_6) of the sulfurization process. For each point in time, β is defined such that $\beta = \pi/2$ represents the stacking sequence denoted in the graphs on the right-hand side.

The left-hand and center graphs reveal that for each point in time, the flipped sequences (with negative β values)

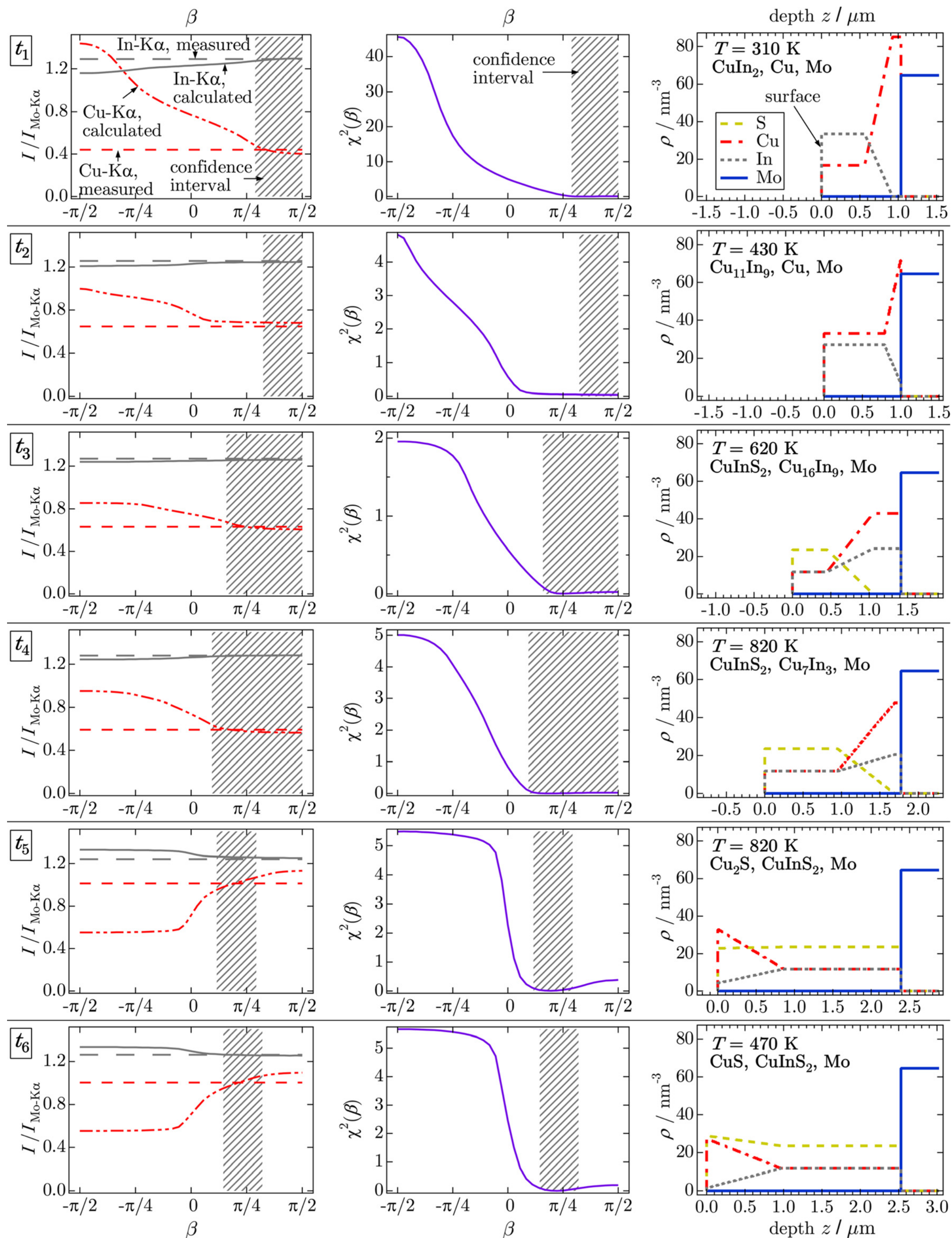

FIG. 10. (Color online) Results of the modeling of elemental depth distributions during the $CuInS_2$ synthesis via reactive annealing of Cu–In precursors in a sulfur atmosphere. t_1 to t_6 denote the points in time marked in Fig. 8. T denotes the substrate temperature measured at these points. (See text for details.)

lead to a large deviation between the calculated and measured fluorescence intensities.

The modeled atomic densities on the right-hand side show the evolution of the elemental depth distribution during the reaction of the metals with sulfur during the reactive annealing process. (The sulfur contents of the sulfur containing layers were calculated from the [S]/([Cu] + [In]) ratio for each phase given by its stoichiometry.) At t_1, the Cu partly stayed at the back of the precursor. A part of the Cu reacted with In to form a $CuIn_2$ layer on top of the Cu layer. After an increase of the substrate temperature to 430 K (t_2), the $CuIn_2$ phase transformed to $Cu_{11}In_9$ by consuming some of the Cu. At 620 K (t_3), the reaction with sulfur started, resulting in the formation of $CuInS_2$ at the top. The elemental Cu was consumed, and the remaining metal phase transferred to $Cu_{16}In_9$. In the following course of the process, the sulfur was further

incorporated into the film (t_4). Due to the Cu excess with respect to the $CuInS_2$ stoichiometry, the consumption of Cu and In with a ratio of 1:1 for the formation of $CuInS_2$ leads to an increase of the [Cu]/[In] ratio of the remaining metal phase (here, Cu_7In_3). Once all of the In is consumed for the formation of $CuInS_2$, Cu_2S forms at the top of the film (t_5). This transition is accompanied by an abrupt increase of the Cu fluorescence signal, as can be seen in Fig. 8(d) between t_4 and t_5. This transition is investigated in detail in the next section. During cooldown, the Cu_2S transforms into the more S-rich phase CuS without significantly influencing the degree of mixing between the copper sulfide phase and the $CuInS_2$ phase. The results presented here are discussed in Sec. IV E.

D. Modeling of Cu diffusion in $CuInS_2$

In this section, we utilize the presented method to derive kinetic values from the *in situ* data. The Cu-Kα signal features a steep increase during the transition of the last remaining metallic phase $Cu_{1-x}In_x$ to the sulfide phase Cu_2S between process time t_4 and t_5, as seen in Fig. 8(d). The evolutions of the signals during the transition are drawn on a larger scale in Figs. 11(b) and 11(d). This increase of the Cu-Kα signal could be modeled by assuming that before the transition the phase $Cu_{1-x}In_x$ is underneath the $CuInS_2$ layer, and after the transition the Cu_2S phase is covering the $CuInS_2$ layer. We conclude that during the transition the excess Cu in the sample diffuses through the $CuInS_2$ layer to the surface of the sample, where it reacts with the sulfur in the gas phase to form Cu_2S.

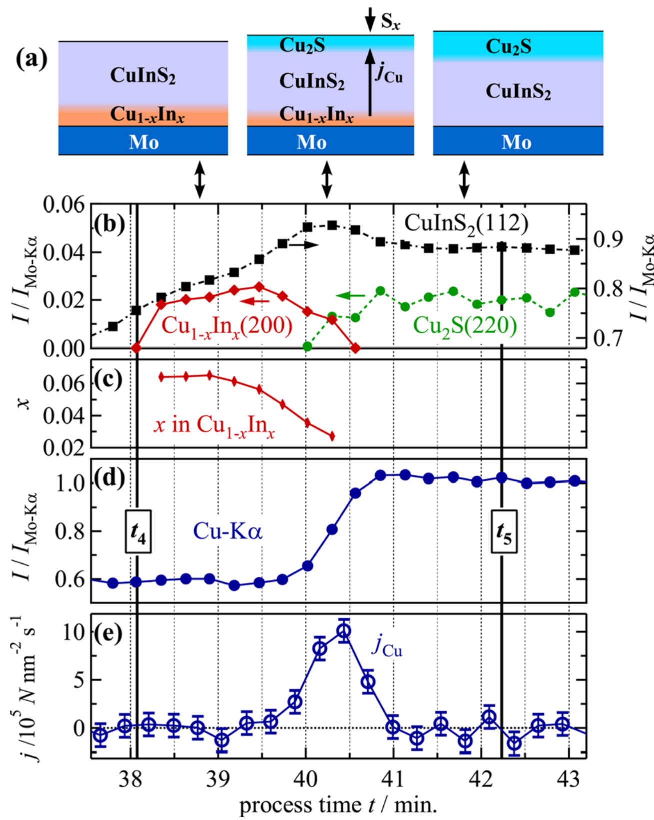

FIG. 11. (Color online) (a) Schematic representation of the Cu diffusion model utilized to simulate the increase of the intensity of Cu-Kα during the transition from $Cu_{1-x}In_x$ (solid solution of In in Cu) to Cu_2S. The In content of $Cu_{1-x}In_x$ was neglected for the modeling. (b) Evolution of measured diffraction signals during the transition from $Cu_{1-x}In_x$ to Cu_2S. The vertical lines labeled with t_4 and t_5 mark the same points in the process time as in Fig. 8. (c) The In content x in $Cu_{1-x}In_x$. The values have been calculated from the energies of the $Cu_{1-x}In_x$ (200) and (110) diffraction signals, assuming an increase of the lattice constant with the In content according to Ref. 47, and assuming a thermal expansion of pure Cu ($\alpha_{Cu} = 1.5 \cdot 10^{-7}\,K^{-1}$). (d) Evolution of measured Cu-Kα fluorescence intensities (relative to Mo-Kα). (e) Modeled current of Cu atom diffusion through the $CuInS_2$ layer from the bottom to the surface. The current gives the number of Cu atoms (N) per area per unit of time. The current is assumed to be uniform throughout the $CuInS_2$ layer. The substrate temperature was 820 K during the shown time interval. The lines connecting the data points serve as guides for the eye.

We derive the current of Cu atoms through the $CuInS_2$ layer and estimate the corresponding diffusion coefficient of Cu in $CuInS_2$ by the use of a four layer model with the stacking order $Cu_2S/CuInS_2/Cu_{1-x}In_x/Mo$. A schematic drawing of the model is presented in Fig. 11(a). As shown in Fig. 11(c), the In content of the $Cu_{1-x}In_x$ phase decreases from 6.5 at.% to 3.5 at.% before the transition to Cu_2S, and further decreases below 3 at.% during the transition. We neglected the *In* content in $Cu_{1-x}In_x$ for the modeling, and therefore denote this phase as Cu in the following.

We calculated the intensity of the Cu-Kα signal as a function of the thickness of the Cu layer for the layer sequence $Cu_2S/CuInS_2/Cu_{1-x}In_x/Mo$. Hereby, the total integral amount of Cu atoms in the sample was kept constant, resulting in an increase of the Cu_2S layer thickness with a decrease of the Cu layer thickness. The thickness could then be expressed as a function of the Cu-Kα intensity. By setting the calculated Cu-Kα intensities equal to the evolution of measured intensities, we obtain the thickness of the Cu layer as a function of the process time. In the following, we use the area density of Cu atoms in the Cu layer, τ_{Cu}, in place of the thickness of the Cu layer.

The current density of Cu atoms diffusing through the $CuInS_2$ layer is the time derivative of the atomic area density τ_{Cu} of Cu atoms in the Cu layer:

$$j_{Cu}(t) = \frac{\Delta\tau_{Cu}}{\Delta t}. \qquad (7)$$

Figure 11(e) shows the time dependent values of the current density $j_{Cu}(t)$ resulting from the calculated values for τ_{Cu} and Eq. (7) (with Δ denoting the difference between two adjacent data points and t being the mean process time between these two data points).

Finally, we estimate the diffusion coefficient of Cu in $CuInS_2$ at the process temperature of 820 K. From Fick's first law, we obtain

$$D = -j_{Cu} \cdot \frac{d_{CIS}}{\Delta c}, \qquad (8)$$

where c is the Cu concentration and d_{CIS} is the thickness of the $CuInS_2$ layer. Assuming a solubility of 3 mol.% In_2S_3 in $CuInS_2$ at 820 K (Ref. 20) and an atom density of 47.1 nm^{-3} for $CuInS_2$ (see Table I), the maximum difference in the copper concentration is $\Delta c = 0.06 \cdot 47.1\,nm^{-3} = 2.8\,nm^{-3}$. With a $CuInS_2$ layer thickness of $d_{CIS} = 2100$nm and a maximum value for the Cu current density $j_{Cu} = 1.0 \cdot 10^6\,nm^{-2}s^{-1}$ (Fig. 11(e)), we obtain

$$D = 7.5 \cdot 10^{-6} \mathrm{cm}^2/\mathrm{s} \tag{9}$$

for the diffusion of Cu in $CuInS_2$ at 820 K. The results are discussed in the following section.

E. Discussion

The calculated fluorescence signals and error squares in Fig. 10 reveal that for each point in time, the measured fluorescence signals are close to the values expected for a layer stack with unmixed, plane-parallel layers consisting of single phases. (We recall that a value of the mixing parameter $\beta = \pi/2$ corresponds to an unmixed, steplike phase sequence, whereas $\beta = 0$ corresponds to a completely homogeneous mixture of two phases.) The match between measurement and calculation can be improved by allowing for some mixing of the phases at their interfaces. However, in some cases, there is a rather large region around the minimum of χ^2 with a rather small dependency of χ^2 on β, resulting in a large confidence interval. Nevertheless, a high degree of layer mixing or a layer sequence with a flipped stacking order can be ruled out with high certainty, due to a significant increase of χ^2 for small and negative values of β.

Our results for the evolution of the depth distributions during $CuInS_2$ synthesis via reactive annealing confirm the results acquired by Calvo-Barrio *et al.* with the help of quenching experiments and *ex situ* measurements.[6] They observed that the chalcopyrite phase grows on top of a metallic phase. The *in situ* results presented in this work reveal that this layer sequence actually exists during the annealing process.

In contrast to process interruptions in combination with *ex situ* measurements, the *in situ* method is suitable for analyzing the diffusion mechanisms occurring during thin film growth processes with a high time resolution. The occurrence of fast Cu diffusion from the back of the sample to the front through the CIS layer, which we used to model the abrupt change of the fluorescence signals (Sec. IV D), has been suggested before[15] and is held responsible for the formation of voids between the Mo layer and the CIS layer. We suspect that the observed voids were filled with Cu before the diffusion of Cu to the front. Our results support this model and additionally provide quantitative kinetic information regarding this procedure. The fact that the In content of $Cu_{1-x}In_x$ (solid solution of In in Cu) decreases before the Cu-Kα signal starts to increase (i.e., before the Cu starts to diffuse to the surface) suggests that In increases the binding energy of Cu in this phase. Only after the In content in $Cu_{1-x}In_x$ drops below 4 at.% (due to the consumption of In for the formation of $CuInS_2$) are the excess Cu atoms released from the $Cu_{1-x}In_x$ phase to form Cu_2S at the surface. The point of Cu_2S formation is, however, influenced by the S activity at the sample surface. Using the presented method, we also studied the influence of the sulfur supply during the annealing process on the Cu diffusion. Establishing the maximum S source temperature already before the beginning of substrate heating leads to an earlier rise of the Cu-Kα signal, accompanied with a simultaneous emergence of the signals for $CuInS_2$ and Cu_2S. This observation can be modeled by an earlier diffusion of the excess Cu to the surface. In this case, no elemental Cu phase was observed at the end of the reaction. This process type results in a reduction of voids between the Mo and CIS layers, which supports the assumption that the diffusion of remaining Cu from the back to the front through the CIS layer is responsible for the void formation between the Mo and CIS layers.

The Cu current and the diffusion coefficient presented in Sec. IV D were derived from measurements on a polycrystalline $CuInS_2$ film, where diffusion via grain boundaries can play a significant role.[33] The diffusion coefficients of Cu in $CuInS_2$ have been determined by Kleinfeld *et al.*[34] for room temperature, with values spanning two orders of magnitude ($D = 5.3 \cdot 10^{-9} \mathrm{cm}^2\mathrm{s}^{-1} \cdots 3.3 \cdot 10^{-7} \mathrm{cm}^2\mathrm{s}^{-1}$). No experimental data for the diffusion coefficient of Cu in $CuInS_2$ at temperatures above room temperature were found in the literature. For the case of the diffusion of Cu in $CuInSe_2$, a wide range of experimental values for diffusion coefficients and temperature dependencies obtained by different methods exist in the literature (results are summarized in Refs. 35 and 36). This is partly due to the fact that the mobility of Cu in chalcopyrite strongly depends on the density of vacancies as well as on grain boundaries. As a consequence, in order to obtain information about the kinetics for a specific reaction process, it is advantageous to derive kinetic values directly from data acquired during the reaction.

For the modeling of the depth distributions presented in this work, the phases were assumed to be stoichiometric. This assumption neglects the fact that the phases may have finite homogeneity ranges. Furthermore, it can be expected that during phase transitions, composition gradients exist within the given homogeneity ranges that act as driving forces for the diffusion of the elements during the phase transitions. However, the widths of the homogeneity ranges for the phases observed in this work lie between 0 and 3 at.% (Refs. 18–21) and are up to 6 at.% for the case of the solid solution $Cu_{1-x}In_x$. In principle, the accuracy of the method can be increased by taking into account possible deviations from the stoichiometric compositions and by using more complex parameterizations of the depth distributions. This would, however, require a sufficiently high resolution of the measured fluorescence intensities and a simultaneous measurement under more than one exit angle.

V. CONCLUSION

We have presented a method for *in situ* depth profiling of elemental distributions by combining the evaluation of x-ray fluorescence with x-ray diffraction, measured by the use of polychromatic synchrotron radiation and a single energy-dispersive detector. The determination of elemental depth distributions during the synthesis of polycrystalline $CuInS_2$ via the reactive annealing of metallic precursors confirmed previous results obtained with quenching experiments and *ex situ* measurements. Additionally, we used the presented method to model the diffusion of Cu through $CuInS_2$ at high temperatures during the synthesis process. According to our model, the excess Cu in the film stays at the back until the formation of $CuInS_2$ is completed. We determined the

decrease of the In content of the metallic Cu–In phase from an energy shift of the corresponding diffraction signals. As soon as In is completely consumed for the formation of $CuInS_2$, Cu diffuses through the $CuInS_2$ layer within 60 seconds to form Cu_2S at the surface. We determined a time-resolved current of Cu atoms through the $CuInS_2$ layer at a process temperature of 830 K by comparing calculated with measured fluorescence intensities. The method as presented here can be applied to various similar problems.

ACKNOWLEDGMENTS

The help of J. Klaer, B. Bunn, and N. Blau in the preparation of precursor samples is gratefully acknowledged. The authors thank Cornelia Streeck for a critical reading of the manuscript. *In situ* measurements have been made possible by the staff at the HASYLAB synchrotron facility and the help of Dr. T. Wroblewski at the beamline F3.

APPENDIX A: CALCULATION OF FLUORESCENCE INTENSITIES FOR FILMS WITH COMPOSITION GRADIENTS

A. Primary fluorescence

For a homogeneous sample and monochromatic excitation, the primary fluorescence intensity can be calculated analytically.[37–40] The probability that a photon of energy $h\nu_{in}$ hitting the sample surface at an angle of θ_{in} will get absorbed within the sample by an atom of an element (denoted by l') and that subsequently this atom will emit a $K\alpha$ fluorescence photon of energy $h\nu_{K\alpha,l'}$ that leaves the sample at an angle θ_{out} is given by

$$W^{\mathrm{I,homo}}_{K\alpha,l'}(\nu_{in},\theta_{in},\theta_{out}) = qH(\nu_{in}-\nu_{K,l'})J_{l'}g_{K\alpha,l'}\omega_{l'} \times\left(1-\exp\left[-\Delta z\sum_l\left[\rho_l\left(\frac{\sigma_l(\nu_{in})}{\sin(\theta_{in})}+\frac{\sigma_l(\nu_{K\alpha,l'})}{\sin(\theta_{out})}\right)\right]\right]\right) \times\sigma_{l'}(\nu_{in})\rho_{l'}\frac{1}{\Sigma_l[\sigma_l(\nu_{in})\rho_l]+[\sin(\theta_{in})/\sin(\theta_{out})]\Sigma_l[\sigma_l(\nu_{K\alpha,l'})\rho_l]}. \tag{A1}$$

Here, the index $K\alpha, l'$ denotes the fluorescence line $K\alpha$ of a certain element l' (the probabilities for $K\beta$ are obtained accordingly). The index l denotes any element in the sample, so that the sums over l sum over all of the elements present in the sample. (In the case treated in the present work, l' or l can denote any of the elements S, Cu, Mo, or In). ρ_l and σ_l are the atomic density and atomic cross-section of element l. Δz is the thickness of the sample. q is a geometry factor that cancels out, because we treat relations of different fluorescence intensities. $H(\nu_{in}-\nu_{K,l'})$ is a step function that ensures that $W^{\mathrm{I,homo}}_{K\alpha,l'}(\nu_{in},\theta_{in},\theta_{out}) = 0$ if the energy of the incident photon $h\nu_{in}$ is below the energy $h\nu_{K,l'}$ of the absorption edge of the K-shell of element l'. The constant $J_{l'}$ is the probability that a photon that is absorbed by element l' will ionize the K-shell of that element (the common label K is dropped here for simplicity). $g_{K\alpha,l'}$ is the probability that the $K\alpha$ transition will be the subsequent transition of an electron filling the K-shell, and $\omega_{l'}$ is the probability that this transition will lead to the emission of a photon. Values for the material parameters were taken from the following references: $g_{K\alpha}$: Ref. 41; ω, $\sigma(\nu)$, ν_K, $\nu_{K\alpha}$: Ref. 42; J: calculated from Ref. 42.

In order to calculate the fluorescence intensities for samples with depth dependent composition variations, the sample is divided into sublayers, where each sublayer is plane-parallel to the surface of the sample and has a uniform composition. (It is pointed out that the division in sublayers done here is different from the allocation of single phases into layers, and that the number of sublayers can be arbitrarily large in order to increase the accuracy of the numerical calculation.) The probability that a photon of energy $h\nu_{in}$ will reach a certain sublayer i is then (according to Lambert's law)

$$W^{\mathrm{trans}}_{i'}(\nu_{in},\theta_{in}) = \exp\left[-\sum_{i=1}^{i'-1}\left[\sum_l[\sigma_l(\nu_{in})\rho_{l,i}]\cdot\frac{\Delta z_i}{\sin(\theta_{in})}\right]\right], \tag{A2}$$

where θ_{in} is the angle between the incoming radiation and the surface, Δz_i is the thickness of sublayer i, and $\rho_{l,i}$ is the atomic density of element l in sublayer i. The sum over i sums over all sublayers up to sublayer i'. To obtain the probability that a photon emitted in a sublayer i' will reach the surface and leave the sample, in Eq. ((2)) the angle θ_{in} simply has to be replaced by the angle θ_{out}, and the photon frequency ν_{in} has to be replaced by the frequency of the emitted fluorescence photon $\nu_{K\alpha,l'}$. To obtain the total primary fluorescence intensity, we multiply Eq. ((1)) with $W^{\mathrm{trans}}_{i'}(\nu_{in},\theta_{in})$ and $W^{\mathrm{trans}}_{i'}(\nu_{K\alpha,l'},\theta_{out})$ from Eq. ((2)), sum over all sublayers i', multiply by the intensity of the polychromatic incident radiation $I_0(\nu_{in})$, and integrate over the energy ν_{in}. For the numerical treatment, the integration is replaced by a sum over discrete intensity intervals, where $\nu_{in,k}$ denotes the mean photon frequency and $I_0(\nu_{in,k})$ the intensity of interval k:

$$I^{\mathrm{I}}_{K\alpha,l'}(\theta_{in},\theta_{out}) \approx \sum_{k=k_{min}}^{k_{max}} I_0(\nu_{in,k})\sum_{i'=1}^{i_{max}} W^{\mathrm{trans}}_{i'}(\nu_{in,k},\theta_{in}) \times W^{\mathrm{I,homo}}_{K\alpha,l',i'}(\nu_{in,k},\theta_{in},\theta_{out})\cdot W^{\mathrm{trans}}_{i'}(\nu_{K\alpha,l'},\theta_{out}). \tag{A3}$$

The maximum incident photon energy taken into account for our calculations was $h\nu_{in,k_{max}} = 150\,\mathrm{keV}$, and the minimum energy was that of the absorption edge of the K-shell of Cu. For the calculation of the fluorescence intensities, the differences between the total cross-sections and the cross-section for photon absorption is neglected. This is justified by the fact that in the energy range of the incident radiation, the contribution of the scattering cross-sections is two to three orders of magnitude smaller than that of the total cross-sections.[42] For the calculation of fluorescence intensities for this work, we chose a total number of $i_{max} = 200$ sublayers.

B. Secondary fluorescence

The secondary fluorescence has been calculated by several authors for homogeneous samples[37,43] and by Mantler for multi-layered samples.[44] Starting from the ansatz of

Mantler, de Boer has introduced the exponential-integral function to handle intra- and interlayer secondary fluorescence.[45] We simply replace the calculation of the intralayer secondary fluorescence by choosing a sufficiently small thickness of the sublayers such that the contribution of intralayer excitation becomes negligible.

For the calculation of the secondary fluorescence, two different sublayers and two different elements are involved: the incident photon gets absorbed by an atom of element l'' in sublayer i'', the subsequently emitted intermediate fluorescence photon gets absorbed by another atom of element l' in layer i', and the fluorescence photon emitted from that atom finally leaves the sample. Following the derivation in Ref. 40 for the intensity of the secondary fluorescence for homogeneous samples, we extended it for samples with depth dependent compositions and for polychromatic excitation:

$$
\begin{aligned}
I^{\mathrm{II}}_{\mathrm{K}\alpha,l'}(\theta_{\mathrm{in}},\theta_{\mathrm{out}})
&= \sum_{k=k_{\min}}^{k_{\max}} I_0(\nu_{\mathrm{in},k}) \sum_{i'=1}^{i_{\max}} \sum_{i''=1}^{i_{\max}} H(\nu_{\mathrm{in},k}-\nu_{\mathrm{K},l''}) \\
&\times J_{l''} g_{\mathrm{K}\alpha,l''}\omega_{l''}\sigma_{l''}(\nu_{\mathrm{in},k})\rho_{l'',i''}\frac{\Delta z_{i''}}{\sin(\theta_{\mathrm{in}})} \\
&\times \int_1^{\infty}\frac{\mathrm{d}t}{t}\exp\left(-\sum_{\substack{i \text{ between}\\ i' \text{ and } i''}}\left[\sum_l [\sigma_l(\nu_{\mathrm{K}\alpha,l''})\rho_{l,i}]\Delta z_i\right]t\right) \\
&\times \frac{1}{2} q H(\nu_{\mathrm{K}\alpha,l''}-\nu_{\mathrm{K},l'}) J_{l'} g_{\mathrm{K}\alpha,l'}\omega_{l'}\sigma_{l'}(\nu_{\mathrm{K}\alpha,l''})\rho_{l',i'}\Delta z_{i'} \\
&\times \exp\left(-\sum_{i=1}^{i''}\left[\sum_l [\sigma_l(\nu_{\mathrm{in},k})\rho_{l,i}]\frac{\Delta z_i}{\sin(\theta_{\mathrm{in}})}\right]\right) \\
&\times \exp\left(-\sum_{i=1}^{i'}\left[\sum_l [\sigma_l(\nu_{\mathrm{K}\alpha,l'})\rho_{l,i}]\frac{\Delta z_i}{\sin(\theta_{\mathrm{out}})}\right]\right). \qquad \text{(A4)}
\end{aligned}
$$

Here, the integration over $t := 1/\sin\theta''$ replaces the integration over all angles θ'' between the direction of flight of the intermediate photon and the surface plane. For the numerical calculation of the integral over t, we rewrite the integral:

$$\int_1^{\infty}\frac{\mathrm{e}^{-at}}{t}\mathrm{d}t = -\int_{-\infty}^{-a}\frac{\mathrm{e}^{y}}{y}\mathrm{d}y, \qquad \text{(A5)}$$

with the substitution $y = -at$. The integral can be decomposed in a series:[46]

$$-\int_{-\infty}^{-a}\frac{\mathrm{e}^{y}}{y}\mathrm{d}y = -\left(C + \ln|a| + \sum_{m=1}^{\infty}\frac{(-a)^m}{m\cdot m!}\right), \qquad \text{(A6)}$$

where C is the Euler constant. In the numerical calculations for the present work, the summation over m was stopped after a relative accuracy of 0.001 was reached. The number of necessary summations needed to reach this accuracy strongly depends on the size of a.

A systematical deviation between calculated and measured fluorescence intensities occurs due to the fact that not all intensity influencing factors are accounted for by the theoretical formulas. These influences—such as the energy dependent detector response, deviations of the incident photon spectrum from the theoretical curve, absorption by the vacuum and nonvacuum beam paths, and systematic deviations of the amounts of elements in the sample from the measured values—are considered by a constant factor $\kappa_{\mathrm{K}\alpha,l'}$ for each fluorescence signal: $I_{\mathrm{K}\alpha,l'} = \kappa_{\mathrm{K}\alpha,l'}(I^{\mathrm{I}}_{\mathrm{K}\alpha,l'} + I^{\mathrm{II}}_{\mathrm{K}\alpha,l'})$. The values for $\kappa_{\mathrm{K}\alpha,l'}$ were determined by fitting calculated intensities to the measured intensities. The values used for the calculations in this work were $\kappa_{\mathrm{K}\alpha,\mathrm{Cu}} = 0.48$, $\kappa_{\mathrm{K}\alpha,\mathrm{Mo}} = 1$, and $\kappa_{\mathrm{K}\alpha,\mathrm{In}} = 1.38$.

Equation (A4) gives the correct result only if sublayer 2, which absorbs the intermediate photon, is of infinite lateral dimension. However, the area seen by the detector is finite. The fraction of the secondary fluorescence that is emitted outside the volume seen by the detector (detector volume) causes a deviation between measurement and calculation. We estimated an upper limit of this error by calculating the fraction of parallel emitted, intermediate radiation that leaves the detector volume. According to this estimation, the error for the calculation of the secondary fluorescence intensity due to the assumption of a layer of infinite lateral dimension is smaller than 4%.

APPENDIX B: CRYSTALLOGRAPHIC PROPERTIES

A. Calculation of atomic area densities

The films investigated in this work had two elements with fixed amounts: Cu and In (the amount of S is a result of the reaction with the metals). If two phases are present, the distribution of Cu and In onto these phases can be calculated (see Sec. III). We did this as described in the following.

We denote the relative amounts for each element l in a phase n by $a_{n,l}$ (e.g., for $CuIn_2$, $a_{\mathrm{CuIn_2,Cu}} = 1$ and $a_{\mathrm{CuIn_2,In}} = 2$; for Cu, $a_{\mathrm{Cu,Cu}} = 1$ and $a_{\mathrm{Cu,In}} = 0$). We further denote the atomic area density for atoms belonging to element l and phase n by $\tau_{n,l}$. The relation of the atomic area densities for two elements l' and l'' within a phase is then given by

$$\frac{\tau_{n,l'}}{\tau_{n,l''}} = \frac{a_{n,l'}}{a_{n,l''}}. \qquad \text{(B1)}$$

For the case of the phase $CuIn_2$, we would obtain $\tau_{\mathrm{CuIn_2,Cu}}/\tau_{\mathrm{CuIn_2,In}} = 1/2$. For a given set of phases, we want to determine the amount of atoms of each element l in each phase n, expressed by the atomic area density $\tau_{n,l}$. The total atomic area density of all atoms of an element in the whole sample is the sum of the atomic area densities within the phases: $\tau_{\mathrm{tot},l} = \Sigma_n\tau_{n,l}$. These conditions, together with the conditions in Eq. (B1), form a set of $N\cdot(\frac{1}{2}L\cdot(L-1)) + L$ linear equations with which $\tau_{n,l}$ can be determined (N is the total number of phases and L is the total number of elements). However, only $N\cdot(L-1)+L$ of these equations are linearly independent. In order to find a set of linearly independent equations, for each of the N phases we have to select one $a_{n,l}$ that is $\neq 0$. For two phases A and B containing the elements Cu and In, after choosing a linear set of equations, we obtain the matrix equation

$$\begin{pmatrix} 1 & 1 & 0 & 0 \\ 0 & 0 & 1 & 1 \\ a_{A,In} & 0 & -a_{A,Cu} & 0 \\ 0 & a_{B,In} & 0 & -a_{B,Cu} \end{pmatrix} \begin{pmatrix} \tau_{A,Cu} \\ \tau_{B,Cu} \\ \tau_{A,In} \\ \tau_{B,In} \end{pmatrix} = \begin{pmatrix} \tau_{tot,Cu} \\ \tau_{tot,In} \\ 0 \\ 0 \end{pmatrix}.$$

The integrated atomic densities for Cu and In of the samples investigated in this work were $\tau_{tot,Cu} = 3.7 \cdot 10^4\ nm^{-2}$ and $\tau_{tot,In} = 2.5 \cdot 10^4\ nm^{-2}$ (calculated from weighing results).

[1]S. Niki, M. Contreras, I. Repins, M. Powalla, K. Kushiya, S. Ishizuka, and K. Matsubara, Prog. Photovoltaics **18**, 453 (2010).
[2]C. Kaufmann, T. Unold, D. Abou-Ras, J. Bundesmann, A. Neisser, R. Klenk, R. Scheer, K. Sakurai, and H.-W. Schock, Thin Solid Films **515**, 6217 (2007).
[3]I. Repins, M. A. Contreras, B. Egaas, C. DeHart, J. Scharf, C. L. Perkins, B. To, and R. Noufi, Prog. Photovoltaics **16**, 235 (2008).
[4]S. Merdes, R. Mainz, J. Klaer, A. Meeder, H. Rodriguez-Alvarez, H. W. Schock, M. C. Lux-Steiner, and R. Klenk, Sol. Energy Mater. Sol. Cells **95**, 864 (2011).
[5]R. Mainz, F. Streicher, D. Abou-Ras, S. Sadewasser, R. Klenk, and M. C. Lux-Steiner, Phys. Status Solidi A **206**, 1017 (2009).
[6]L. Calvo-Barrio, A. Perez-Rodriguez, A. Romano-Rodriguez, B. Barcones, J. R. Morante, K. Siemer, I. Luck, and R. Klenk, Vacuum **63**, 315 (2001).
[7]A. Neisser, I. Hengel, R. Klenk, T. W. Matthes, J. Álvarez García, A. Pérez-Rodríguez, A. Romano-Rodríguez, and M. C. Lux-Steiner, Sol. Energy Mater. Sol. Cells **67**, 97 (2001).
[8]T. Rissom, R. Mainz, C. A. Kaufmann, R. Caballero, V. Efimova, V. Hoffmann, and H.-W. Schock, Sol. Energy Mater. Sol. Cells **95**, 250 (2011).
[9]C. Streeck, B. Beckhoff, F. Reinhardt, M. Kolbe, B. Kanngießer, C. Kaufmann, and H. Schock, Nucl. Instrum. Methods Phys. Res. B **268**, 277 (2010).
[10]C. von Klopmann, E. Djordjevic, J. Rudigier, and R. Scheer, J. Cryst. Growth **289**, 121 (2006).
[11]K. Ellmer, R. Mientus, V. Weiss, and H. Rossner, Meas. Sci. Technol. **14**, 336 (2003).
[12]C. von Klopmann, J. Djordjevic, and R. Scheer, J. Cryst. Growth **289**, 113 (2006).
[13]J. Djordjevic, E. Rudigier, and R. Scheer, J. Cryst. Growth **294**, 218 (2006).
[14]R. Mainz, R. Klenk, and M. Lux-Steiner, Thin Solid Films **515**, 5934 (2007).
[15]H. Rodriguez-Alvarez, I. Koetschau, C. Genzel, and H. Schock, Thin Solid Films **517**, 2140 (2009).
[16]H. Rodriguez-Alvarez, I. Kötschau, and H. Schock, J. Cryst. Growth **310**, 3638 (2008).
[17]A. Weber, R. Mainz, and H. W. Schock, J. Appl. Phys. **107**, 013516 (2010).
[18]A. Bolcavage, S. W. Chen, C. R. Kao, Y. A. Chang, and A. D. Romig, J. Phase Equilib. **14**, 14 (1993).
[19]S. Fiechter, Y. Tomm, M. Kanis, R. Scheer, and w. Kautek, Phys. Stat. Sol. (b) **245**, 1761 (2008).
[20]J. J. M. Binsma, L. J. Giling, and J. Bloem, J. Cryst. Growth **50**, 429 (1980).
[21]D. Chakrabarti and D. Laughlin, Bull. Alloy Phase Diagrams **2**, 305 (1981).
[22]F. Laves and H. Wallbaum, Z. Angew, Mineral. **4**, 17 (1942).
[23]S. Fiechter, Y. Tomm, M. Kanis, R. Scheer, and W. Kautek, Phys. Status Solidi B **245**, 1761 (2008).
[24]H. Swanson and E. Tatge, Natl. Bur. Stand. Circ. (U.S.) **539**, 1 (1953).
[25]J. F. Smith and V. Schneider, J. Less-Common Met. **7**, 17 (1964).
[26]W. Keppner, T. Klas, W. Körner, R. Wesche, and G. Schatz, Phys. Rev. Lett. **54**, 2371 (1985).
[27]T. P. Rajasekharan and K. Schubert, Z. Metallkd. **72**, 275 (1981).
[28]A. S. Koster, L. R. Wolff, and G. J. Visser, Acta Crystallogr., Sect. B: Struct. Crystallogr. Cryst. Chem. **36**, 3094 (1980).
[29]H. Hahn, G. Frank, W. Klingler, A.-D. Meyer, and G. Störger, Z. Anorg. Allg. Chem. **271**, 153 (1953).
[30]H. Fjellvag, F. Gronvold, S. Stolen, A. F. Andresen, and R. Müller-Käfer, Z. Kristallogr. **184**, 111 (1988).
[31]M. Oliveria, R. K. McMullan, and B. J. Wuensch, Solid State Ionics **28**, 1332 (1988).
[32]R. Mainz, In-situ Analyse und Wachstum photovoltaischer Absorber mit Bandlueckengradienten, °Ph.D. dissertation (Freie Universität Berlin, Germany, 2008).
[33]A. Neisser, Gallium as an Isovalent Substitution in CuInS2 Absorber Layers for Photovoltaic Applications, °Ph.D. dissertation (Freie Universität Berlin, Germany, 2001).
[34]M. Kleinfeld and H. D. Wiemhöfer, Solid State Ionics **28–30**, 1111 (1988).
[35]I. Lubomirsky, K. Gartsman, and D. Cahen, J. Appl. Phys. **83**, 4678 (1998).
[36]J. Pohl and K. Albe, J. Appl. Phys. **108**, 023509 (2010).
[37]E. Gillam and H. T. Heal, Br. J. Appl. Phys. **3**, 353 (1952).
[38]H. Beattie and R. Brissey, Anal. Chem. **26**, 980 (1954).
[39]R. O. Müller, *Spectrochemical Analysis by X-Ray Fluorescence* (Hilger, London, 1972).
[40]R. Tertian and F. Claisse, *Principles of Quantitative X-Ray Fluorescence Analysis* (John Wiley & Sons Ltd., New York, 1982).
[41]J. S. Hansen, H. U. Freund, and R. W. Fink, Nucl. Phys. A **142**, 604 (1970).
[42]W. H. McMaster, N. K. D. Grande, J. H. Mallett, and J. H. Hubbell, Compilation of X-Ray Cross Sections (National Technical Information Services L-3, 1969).
[43]T. Shiraiwa and N. Fujino, Jpn. J. Appl. Phys. **5**, 886 (1966).
[44]M. Mantler, Anal. Chim. Acta **188**, 25 (1986).
[45]D. K. G. de Boer, X-Ray Spectrom. **19**, 145 (1990).
[46]I. N. Bronstein, K. A. Semendjajew, G. Musiol, and H. Mühlig, *Taschenbuch der Mathematik, 3. Auflage* (Verlag Harri Deutsch, Frankfurt am Main, 1997).
[47]P. Subramanian and D. Laughlin, Bull. Alloy Phase Diagrams **10**, 554 (1989).